# Development and Preliminary Verification of a Neutronics-Thermal Hydraulics Coupling Code for Research Reactors with Unstructured Meshes

Mingrui Yang[1], Chixu Luo[1], Dan Wang[2], Tianxiong Wang[2], Xiaojing Liu[1], and Tengfei Zhang[1](✉)

[1] Shanghai Jiao Tong University, Shanghai, China
{yangmr96,zhangtengfei}@sjtu.edu.cn
[2] Nuclear Power Institute of China, Chengdu, Sichuan, China

**Abstract.** To maximize their adaptability and versatility, research reactors are designed to adapt to various operational conditions. These requirements result in more complex configurations and irregular geometries for research reactors. Besides, there is usually a strong coupling of neutronics-thermal hydraulics (N-TH) fields inside the reactor. A three-dimensional N-TH coupling code has been developed named CENTUM (CodE for N-Th coupling with Unstructured Mesh). Steady-state and transient neutronic analyses are performed using a 3D triangular-z nodal transport solver with the stiffness confinement method (SCM). Meanwhile, thermal-hydraulics calculations adopt a multi-channel model. For a preliminary verification of the code, we examine CENTUM with benchmark problems including TWIGL, 3D-LMW, and NEACRP. CENTUM produces maximum power errors of −1.27% and −0.45% for the TWIGL A1 and A2 cases, respectively. For the 3D-LMW benchmark, the largest relative power error of 3.84% is observed at 10 s compared with the reference SPANDEX code. For the NEACRP N-TH coupling benchmark, CENTUM results in a 0.35 ppm error in critical boron concentration, a 2.16 °C discrepancy in the fuel average Doppler temperature, and a 0.63% overestimation in the maximum axial power. Moreover, transient results considering thermal-hydraulics feedback are in good agreement with the PARCS reference solutions, with the maximum relative power deviation being only 0.055%.

**Keywords:** Reactor Kinetics · Stiffness Confinement Method · Neutronics-Thermal Hydraulics Coupling · Safety Analysis · Research Reactor

## 1 Introduction

Research reactors have served as the workhorse for nuclear fuel and material irradiation testing, and they can also be used for secondary missions such as isotope production and electricity generation. They serve as research, development, and demonstration platforms for fuels, materials, and other critical components. To maximize their adaptability and

© The Author(s) 2023
C. Liu (Ed.): PBNC 2022, SPPHY 283, pp. 673–689, 2023.
https://doi.org/10.1007/978-981-99-1023-6_58

versatility, research reactors are designed to adapt to a variety of operational conditions. These requirements result in more complex configurations and irregular geometries for research reactors than for conventional Pressurized Water Reactors (PWRs) and Boiling Water Reactors (BWRs). Direct application of conventional reactor analysis codes to research reactors is challenging due to their complex geometrical configurations and high neutron streaming caused by frequent control rod movement. It is noted that geometry complexity is a feature shared by almost all research reactors, which limits the feasibility of conventional methods based on rectangular or hexagonal meshes. As a result, the ability to accurately model research reactors require the ability to describe unstructured meshes. Additionally, the local neutron spectrum in a research reactor varies significantly with position, and frequent control rod operation results in significant neutron flux heterogeneity. Therefore, it is required to solve the neutron transport equation that can describe the angular anisotropy and to take into account the coupling of various physical fields in order to accurately simulate the behavior of the reactor. This will surely use a lot of computational resource during the core's transient analysis. However, due to the physical nature of the reactor, the use of conventional numerical methods, such as implicit Euler method [1] and Runge-Kutta methods [2], encounters serious problems due to the "rigidity" of the set of equations. Solving with these methods requires very small time-step sizes in order to ensure the stability of the method, and thus many unnecessary information will be computed while the computation continues for long transition times, leading to a huge waste of computational resources, and may also contain large cumulative errors. The precursor concentration equation introduced stiffness into the system, so we employ the stiffness confinement method (SCM) technique to decouple the neutron flux density equation and the delayed neutron density equation, eliminating the stiffness introduced by the precursor concentration equation [3].

Due to the strong coupling between reactor neutronics and thermal hydraulics, a multi-channel model is used to describe the coolant convection and the finite difference method to calculate the thermal conductivity of the fuel rods, so as to provide feedback on the cross-section used for the neutronics calculation. CENTUM's adopts the OSSI [4] (Operator Splitting Semi-Implicit) method for coupling. Figure 1 depicts the coupling flow of the OSSI method. Each time step begins with a neutronics calculation, and the power rate for each assembly is transferred to the thermal hydraulics module. Without iterating, the process enters directly to the next time step after the thermal hydraulics calculation is finished.

This paper is organized as follows. Section 2 illustrates the steady-state triangular-z node neutron transport model, the transient SCM method and the thermal hydraulics models embedded in CENTUM. As a preliminary verification, Sect. 3 presents numerical verification results using TWIGL, LMW and NEACRP benchmark cases. Specifically, the TWIGL benchmark and the LMW benchmark are neutronics transient problems, and the NEACRP is a problem to demonstrate CENTUM's capability of modeling the N-TH coupling effect.

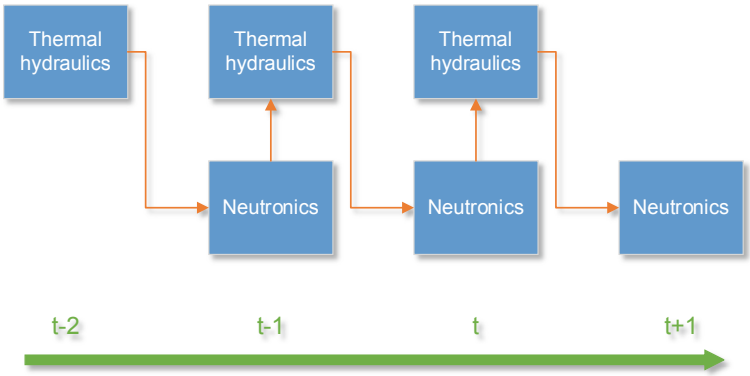


**Fig. 1.** The OSSI method in CENTUM

## 2 Methodology

### 2.1 Triangular-Z Node Neutron Transport Model

Considering isotropic scattering and using $S_N$ method, the three-dimensional multi-group neutron transport equation in the triangular prism can be written as [5]:

$$\mu^m \frac{\partial \Psi_g^m(x,y,z)}{\partial x} + \eta^m \frac{\partial \Psi_g^m(x,y,z)}{\partial y} + \frac{\xi^m}{h_z}\frac{\partial \Psi_g^m(x,y,z)}{\partial z} + \Sigma_t^g \varphi_g^m(x,y,z) = \hat{Q}_g(x,y,z) \tag{2.1}$$

Here, $\mu^m$, $\eta^m$, $\xi^m$ are the components of the angular direction m on the x, y, z axes; m is a certain angular direction after using $S_N$ discretization; $\hat{Q}_g(x,y,z)$ is The neutron source term includes fission sources and scattering sources ($cm^{-3}\cdot s^{-1}$); $\Psi_g^m$ represents the neutron angular flux density of the g group in the m direction ($cm^{-2}\cdot s^{-1}$). Usually, the solved triangular node is arbitrary, and it needs to be transformed into a unified coordinate system (Fig. 2).

Using the coordinate transformation, we obtain the equation as:

$$\begin{aligned}&\mu_x^m \frac{\partial \psi_g^m(x',y',z)}{\partial x'} + \eta_x^m \frac{\partial \psi_g^m(x',y',z)}{\partial y'} + \frac{\xi^m}{h_z}\frac{\partial \psi_g^m(x',y',z)}{\partial z} + \Sigma_t^g \psi_g^m(x',y',z)\\ &= Q_g(x',y',z)\end{aligned} \tag{2.2}$$

where

$$\mu_x^m = \frac{(-y_n + y_p)\mu^m + (x_n - x_p)\eta^m}{2\Delta}$$

$$\eta_x^m = \frac{(-x_k + \frac{1}{2}x_n + \frac{1}{2}x_p)\eta^m + (y_k - \frac{1}{2}y_n - \frac{1}{2}y_p)\mu^m}{\sqrt{3}\Delta}$$

$$-2/3 \le x' \le 1/3,\quad -y_s(x') \le y' \le y_s(x'),\ y_s(x') = (x' + 2/3)/\sqrt{3},\ -1/2 \le z \le 1/2$$

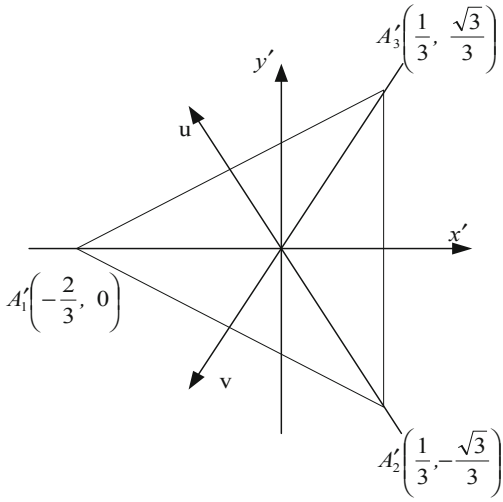


**Fig. 2.** Equilateral triangle in the calculated coordinate system

The nodal balance equation is given by:

$$2\mu_x^m \overline{\psi}_x^m + 2\mu_u^m \overline{\psi}_u^m + 2\mu_v^m \overline{\psi}_v^m + \frac{\xi^m}{h_z}\left(\overline{\psi}_{z+}^m - \overline{\psi}_{z-}^m\right) + \Sigma_t \overline{\psi}^m = \overline{Q} \tag{2.3}$$

$\overline{\psi}_i^m$ is the averaged outgoing surface flux in the x, u, v directions, as is shown in Fig. 1; $\overline{\psi}_{z\pm}^m$ are the outgoing surface averaged flux of the upper and lower sides of the node; $\overline{\psi}^m$ is the averaged flux in the node. The transport computation is performed using a specific sweeping and source iteration approach.

## 2.2 Transient Neutronic Model

For solving transient problems, CENTUM adopts the SCM [6]. By considering that the dynamic frequency of the angular flux is isotropic:

$$\omega_g(r,t) = \frac{\partial}{\partial t} \ln \varphi_g(r,t) \tag{2.4}$$

where $\omega_g(r,t)$ is the flux dynamic frequency of group g; $\varphi_g(r,t)$ is the scalar flux of group g.

The flux dynamic frequency can be further decomposed into the shape frequency $\omega_{s,g}(r,t)$ and the amplitude frequency $\omega_t(t)$.

$$\omega_g(r,t) = \omega_{s,g}(r,t) + \omega_t(t) \tag{2.5}$$

Similarly, the precursor frequency of group $i$ is defined as:

$$\mu_i(r,t) = \frac{\partial}{\partial t} \ln C_i(r,t) \tag{2.6}$$

Inserting (2.4) and (2.6) into the 3-D multigroup time-space neutron transport equation within a triangular-z prism, the time-dependent neutron transport equation can be transformed into an equation for solving the eigenvalue problem:

$$\begin{aligned}&\mu^m \frac{\partial}{\partial x}\varphi_g^m(r,t) + \eta^m \frac{\partial}{\partial y}\varphi_g^m(r,t) + \frac{\xi^m}{h_Z}\frac{\partial}{\partial z}\varphi_g^m(r,t)\\&+\Sigma'_{t,g}(r,t)\varphi_g^m(r,t) = \frac{\chi'_g}{k_D}\sum_{g'=1}^{G}(\nu\Sigma_{\mathrm{f}})_{g'}(r,t)\varphi_g^m(r,t)\\&+\sum_{g'=1}^{G}\varphi_g^m(r,t)\Sigma_{g'\to g}(r,t)\end{aligned} \tag{2.7}$$

$k_D$ is the dynamic eigenvalue; $\Sigma'_{t,g}$ is the dynamic total cross-section and $\chi'_g$ is the dynamic fission spectrum, which are respectively defined as:

$$\Sigma'_{t,g}(r,t) = \Sigma_{t,g}(r,t) + \frac{\omega_g(r,t)}{v_g} \tag{2.8}$$

$$\chi'_g = \chi_g(1-\beta) + \sum_{i=1}^{M}\chi_{ig}\lambda_i\frac{\beta_i}{\mu_i+\lambda_i} \tag{2.9}$$

Here, $v_g$ represents the neutron velocity of the g group. The unknown quantities are the flux dynamic frequency and the precursor frequency. Solving for $k_D$ iteratively by Eq. (2.7), combined with the secant method, we get amplitude frequency:

$$\omega_t^{(m+1)}(t_n) = \omega_t^{(m)}(t_n) + \left[\omega_t^{(m-1)}(t_n) - \omega_t^{(m)}(t_n)\right]\frac{1-k_{\mathrm{D}}^{(m)}}{k_{\mathrm{D}}^{(m-1)} - k_{\mathrm{D}}^{(m)}} \tag{2.10}$$

Based on the isotropic approximation, the average scalar flux in the nodal $\nu$ is used to update the node wise shape frequency:

$$\overline{\omega}_{\nu,S,g}(t_n) = \frac{1}{\Delta t_n}\ln\left[\frac{\int_\nu drf^T(r)\widehat{\varphi}_{\nu,g}(t_n)}{\int_\nu drf^T(r)\varphi_{\nu,g}(t_{n-1})}\right] \tag{2.11}$$

in which $\widehat{\varphi}_{\nu,g}$ is the flux normalized according to the neutron density; $\overline{\omega}_{\nu,S,g}(t_n)$ is the average shape frequency within $[t, t+\Delta t]$. Meanwhile the actual flux can be written as:

$$\varphi_{\nu,g}(r,t) = \widehat{\varphi}_{\nu,g}(r,t)e^{\frac{\omega_T(t_n)+\omega_T(t_{n-1})}{2}\Delta t_n} \tag{2.12}$$

Assume that the precursor concentration is uniform within each node, the analytical solution for the precursor concentration is expressed as:

$$C_{\nu,i}(t_n) = C_{\nu,i}(t_{n-1})e^{-\lambda_i\Delta t_n} + \beta_i e^{-\lambda_i\Delta t_n}\int_{t_{n-1}}^{t_n} Q_\nu(t)e^{\lambda_i t}dt \tag{2.13}$$

where $\beta_i$ is the share of group i precursor, $\lambda_i$ is its decay constant; $Q_\nu$ is the the node-wise fission source. Combined with Eq. (2.13) the precursor frequency can be updated by:

$$\mu_{\nu,i}(t_n) = \begin{cases}\beta_i\frac{Q_\nu(t_n)}{C_{\nu,i}(t_n)} - \lambda_i & C_{\nu,i}(t_n) \neq 0\\ 0 & C_{\nu,i}(t_n) = 0\end{cases} \tag{2.14}$$

After obtaining the flux frequency and the precursor frequency, we can iteratively Solve $k_D$ by adjusting dynamic total cross-section and the dynamic fission spectrum by using Eq. (2.8) and (2.9). The neutronics transient solving process is shown below (Fig. 3).

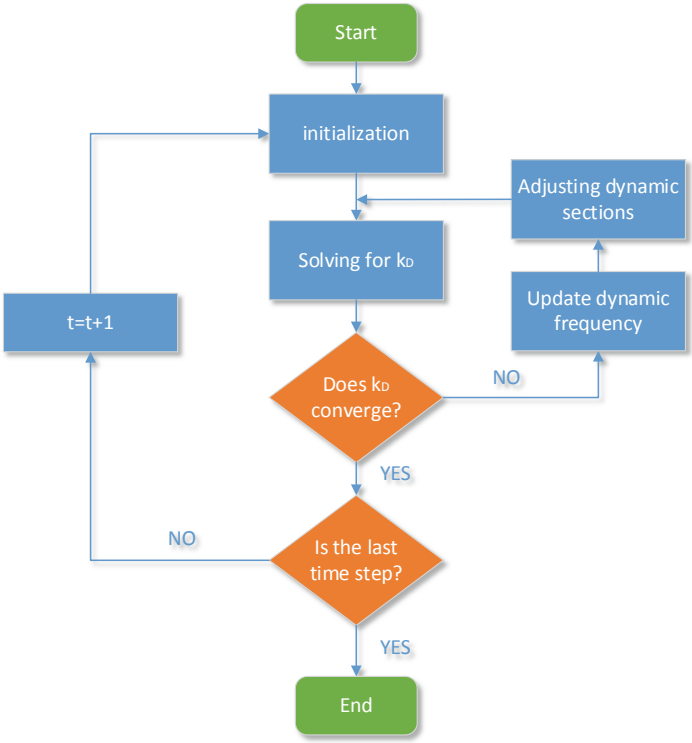


**Fig. 3.** Flowchart of the transient calculations with SCM

## 2.3 Thermal Hydraulics Model

In the N-Th coupling process, the thermal hydraulics calculation is used to obtain the thermal hydraulic parameters of the fuel rods and moderator. These parameters are then used to calculate the effect on the cross-sections used for the neutronics calculations.

### 2.3.1 Moderator Thermal Hydraulics Equation

CENTUM solves the thermal-hydraulics field using multi-channel models. The one-dimensional thermal hydraulics equations are expressed as follows [7]:

Moderator mass conservation equation:

$$\frac{\partial}{\partial t}(\rho)+\frac{\partial}{\partial z}(\rho u) = 0 \tag{2.15}$$

Moderator energy conservation equation:

$$\frac{\partial}{\partial t}(\rho h) + \frac{\partial}{\partial z}(\rho u h) = Q^f \tag{2.16}$$

Moderator momentum conservation equation:

$$\frac{\partial}{\partial t}(\rho u) + \frac{\partial}{\partial z}(\rho u^2) + \frac{\partial P_{fric}}{\partial z} + g\rho + \frac{\partial P}{\partial z} = 0 \tag{2.17}$$

Moderator control equations are solved using a parallel multi-channel model, the flow distribution is based on equal pressure drop in each parallel multi-channel where the inlet and outlet are at the same isobaric surface. The time derivative term is treated with the full-implicit backward difference method and the space variables are treated with the finite difference method.

### 2.3.2 Fuel Rod Heat Transfer Equation

In a one-dimensional cylindrical coordinate system, ignoring the effect of the axial direction, Fuel rod heat transfer equation as shown below [8]:

$$\rho c \frac{\partial T}{\partial t} + \frac{d^2 T}{dr} + \frac{1}{r}\frac{dT}{dr} + \frac{Q}{\lambda} = 0 \tag{2.18}$$

where $T$ is the distribution of temperature; $Q$ is the volumetric heat release rate of the fuel; $\lambda$, $\rho$ and $c$ are the thermal conductivity, density and heat capacity of the fuel material respectively. These properties change with temperature.

The spatial variable in the thermal conductivity equation is treated by the finite difference method. The cylindrical geometry from the inside to the outside are taken successively as the fuel zone, the air gap zone and the cladding zone. For the time discretization, the Crank-Nicholson implicit difference method is used, where $\theta$ equals 0.5 in Eq. (2.19).

$$\begin{aligned} \frac{\partial A(r,t)}{\partial t} &= B(r,t) \\ \frac{A(r,t+\Delta t) - A(r,t)}{\Delta t} &= (1-\theta)B(r,t+\Delta t) + \theta B(r,t) \end{aligned} \tag{2.19}$$

By discretization, the following tridiagonal matrix can be obtained:

$$\begin{pmatrix} b_1 & c_1 & 0 & 0 & \cdots & 0 & 0 \\ a_2 & b_2 & c_2 & 0 & \cdots & 0 & 0 \\ 0 & a_3 & b_3 & c_3 & \ddots & \vdots & \vdots \\ 0 & 0 & \ddots & \ddots & \ddots & 0 & 0 \\ \vdots & \vdots & \ddots & a_{n-2} & b_{n-2} & c_{n-3} & 0 \\ 0 & 0 & \cdots & 0 & a_{n-1} & b_{n-1} & c_{n-1} \\ 0 & 0 & \cdots & 0 & 0 & a_n & b_n \end{pmatrix} \begin{pmatrix} \overline{T_1}^{t+\Delta t} \\ \overline{T_2}^{t+\Delta t} \\ \overline{T_3}^{t+\Delta t} \\ \\ \overline{T_{n-2}}^{t+\Delta t} \\ \overline{T_{n-1}}^{t+\Delta t} \\ \overline{T_n}^{t+\Delta t} \end{pmatrix} = \begin{pmatrix} q_1 \\ q_2 \\ q_3 \\ \\ q_{n-2} \\ q_{n-1} \\ q_n \end{pmatrix} \tag{2.20}$$

in which $n$ is the node number; $a_n$, $b_n$, $c_n$ and $q_n$ are constants related to the geometry, material and the temperature distribution at the previous time step.

## 3 Results and Discussion

The primary purpose of this section is to verify CENTUM's the transient function. TWIGL and LMW benchmark problem are mainly to verify the neutronics model of CENTUM, and NEACRP is to verify the N-Th coupling function. All results are evaluated with the angular discretization order of $S_2$. The triangular-z nodes are generated by Gmsh. All calculations are performed on a personal computer with a 2.90 GHz Intel i7-10700 CPU processor useing serial computation.

### 3.1 TWLGL Benchmark Problem

This section illustrates the preliminary verification of CENTUM using a simplified two-dimensional two-group dynamics benchmark problem with one set of precursor dynamics parameters [9, 10]. The core consists of three fuel zones forming a square core with a side length of 160 cm, and the fuel assembly size is 8 cm × 8 cm. The geometric arrangement of the core is shown in Fig. 4. The outer boundary condition of the original problem is a zero-flux density boundary, and since the transport calculations cannot handle this type of boundary, vacuum boundary conditions are used instead. The total number of triangular meshes used in the calculation is 400 as shown in Fig. 5, with one radial layer, and reflection boundary conditions are set on the upper and lower surfaces.

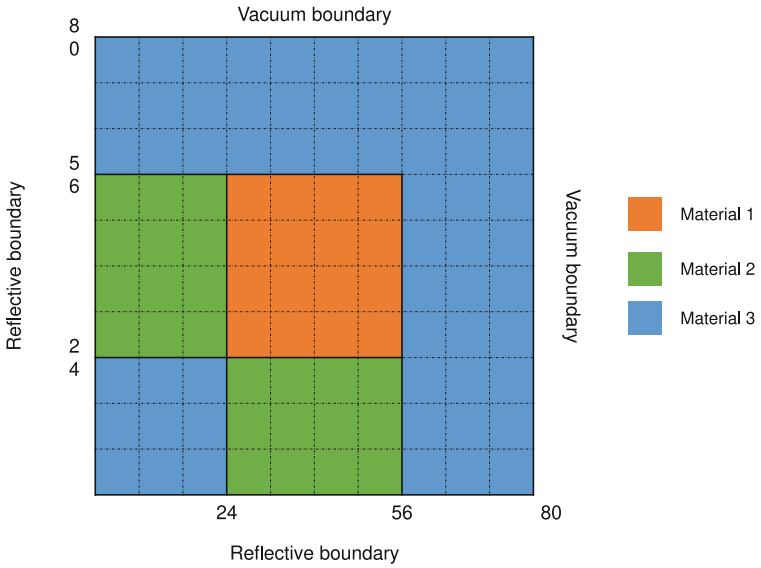


**Fig. 4.** Layout of the TWIGL problem

The calculation area is 1/4 of the core, and the transient process lasts for 0.5 s. The original problem includes two delayed supercritical problems, A1 and A2. The two problems introduce perturbation ramp and stepwise, respectively. For A1 and A2 problems, two sets of reference values are used, one is the transport calculation result

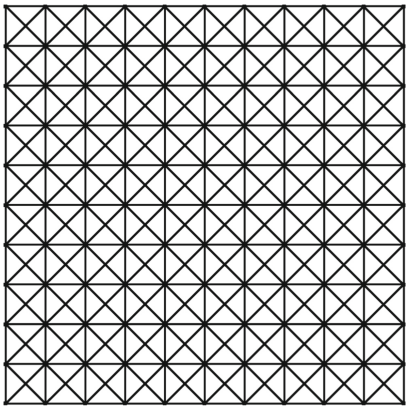

**Fig. 5.** Mesh of TWIGL benchmark in CENTUM

of UTK's improved quasi-static method code TDTORT; the other is the diffusion calculation result of the time direct discrete nodal code SPANDEX which adopts the θ method with a time-step sizes of 0.1 ms [9, 10]. As can be seen from the results in Fig. 6, the results of CENTUM ($S_2$) agree well with TDTORT ($S_4$), while the results of both transport codes are higher than the diffusion code. This discrepancy is mainly due to the zero-flux boundary condition used for the diffusion calculation, which leads to the core internal total power value being slightly smaller for the same perturbation case.

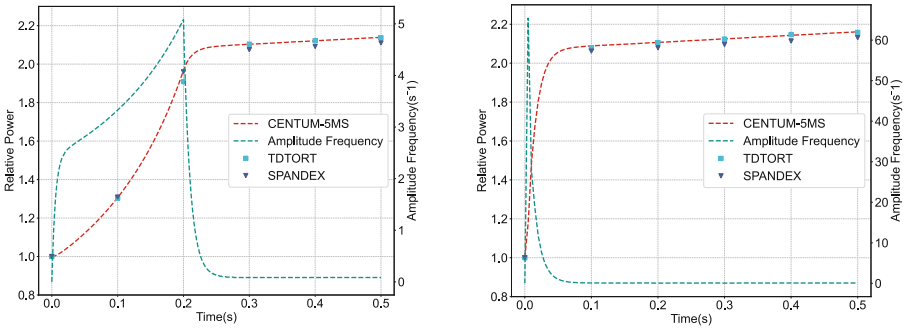


(a) A1 (b) A2

**Fig. 6.** Results of the TWIGL A1, A2 problem

To further compare the effect of time-step sizes on the calculation results, Table 1, Table 2 gives the normalized power values for the A1, A2 problems.

Compared with TDTORT, the results of CENTUM (20 ms) are in good agreement in both cases, the maximum deviation of the A1 case is 3.83%, and the maximum deviation of the A2 case is 0.41%. And the results obtained by CENTUM using the two time-step sizes are consistent, it show that CENTUM ensures acceptable accuracy even with large time-step sizes.

**Table 1.** Comparison of core relative powers for the TWIGL A1 problem

| Time (s) | TDTORT | CENTUM | CENTUM | Err (%) | |
|---|---|---|---|---|---|
| | | $\Delta t = 5$ ms | $\Delta t = 20$ ms | Vs. $\Delta t = 5$ ms | Vs. $\Delta t = 20$ ms |
| 0.0 | 1.000 | 1.000 | 1.000 | 0.00 | 0.00 |
| 0.1 | 1.304 | 1.313 | 1.313 | 0.70 | 0.71 |
| 0.2 | 1.909 | 1.982 | 1.982 | 3.83 | 3.83 |
| 0.3 | 2.104 | 2.103 | 2.103 | −0.03 | −0.03 |
| 0.4 | 2.122 | 2.121 | 2.120 | −0.03 | −0.07 |
| 0.5 | 2.137 | 2.140 | 2.139 | 0.12 | 0.11 |

**Table 2.** Comparison of core relative powers for the TWIGL A2 problem

| Time (s) | TDTORT | CENTUM | CENTUM | Err (%) | |
|---|---|---|---|---|---|
| | | $\Delta t = 5$ ms | $\Delta t = 20$ ms | Vs.$\Delta t = 5$ ms | Vs.$\Delta t = 20$ ms |
| 0.0 | 1.000 | 1.000 | 1.000 | 0.00 | 0.00 |
| 0.1 | 2.079 | 2.089 | 2.087 | 0.46 | 0.41 |
| 0.2 | 2.106 | 2.107 | 2.106 | 0.04 | 0.00 |
| 0.3 | 2.124 | 2.125 | 2.123 | 0.05 | −0.03 |
| 0.4 | 2.147 | 2.143 | 2.141 | −0.18 | −0.26 |
| 0.5 | 2.158 | 2.161 | 2.160 | 0.15 | 0.10 |

In CENTUM, the neutron density of the core is given by Eq. (2.12). The amplitude frequency determines the overall power of the core. From Fig. 7, it can be found that the longer the time step, the more obvious the oscillation of the amplitude frequency.

When the time-step sizes is increased, the solution of the amplitude frequency will deviate more from the true value. CENTUM use the average of the amplitude frequencies at time $t$ and $t+\Delta t$ to approximate the amplitude frequency of the time period $[t, t + \Delta t]$. Affected by this characteristic, when iteratively solves the amplitude frequency at time $t+\Delta t$, it will be affected by the amplitude frequency of the previous time step. Eventually, the amplitude frequency at large time-step sizes fluctuate around the true value. So in the end we can get accurate results as long as the average between the two time steps is close to the true value, this feature can effectively reduce the cumulative error. However, when the time-step sizes is too large and the reactivity changes sharply, the average amplitude frequency at two time points cannot reflect the real change very well.

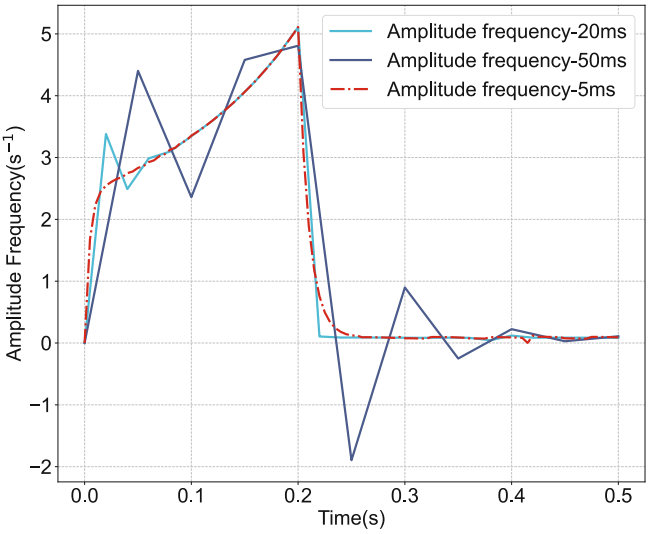


**Fig. 7.** Amplitude frequencies at different time-step sizes in TWIGL A1

### 3.2 3D-LMW Benchmark Problem

The 3D-LMW is a 3D diffusion benchmark [9, 10], which contains six sets of delayed neutron dynamics parameters, and the outer boundary is a vacuum boundary. In this paper, the calculation is performed with a quarter-core model. Figure 8 and 9 depict the problem's radial and axial geometrical arrangements, respectively. The motion of two groups of control rods is what causes the transient process: at the start of the transient, the first group of rods are inserted into the middle of the core at a height of 100 cm from the bottom, and the second group rods are withdraw from the active core; between 0.0 s and 26.666 s, the first group rods were lifted out of the active area of the core at a speed of 3.0 cm/s, and the second group rods were gradually inserted into the core from 7.5 s to 47.5 s. CENTUM uses spatial volume weights to deal with the cuspate effect of the control rods.

The size of the LMW assemblies is 20 cm × 20 cm. In CENTUM calculations, a total of 468 triangular meshes are divided radially, as shown in Fig. 10, and the axial 200 cm is divided into 10 layers. The entire transient process lasts for 60 s, and the reactivity changes during the process are slight, so a large time-step sizes of 0.5 s chosen for calculation.

The calculation results shown in Fig. 11. The two sets of reference solutions used for comparison are diffusion codes. The relative power trend of CENTUM is in good agreement with the reference solution, the largest relative power error of 3.84% occurs at 10s compared with SPANDEX [9, 10]. However, at this time step, the deviation between SPANDEX and SIMULATE is also quite significant. Likewise, this difference attributed to the discrepancy between the transport method and the diffusion method.

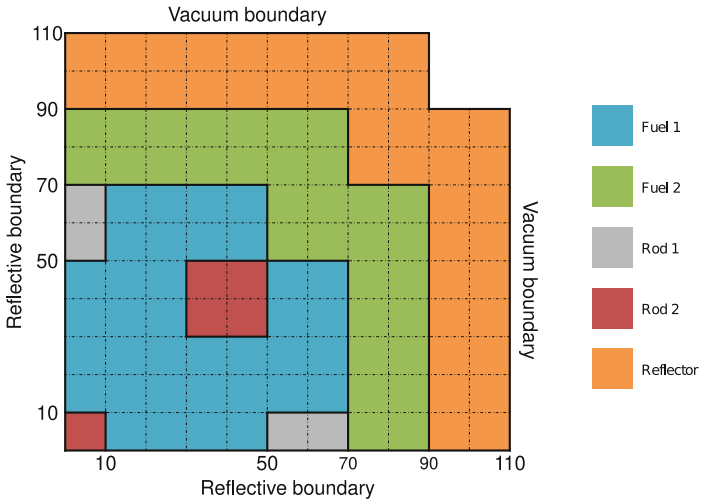


**Fig. 8.** Radial layout of the LMW problem

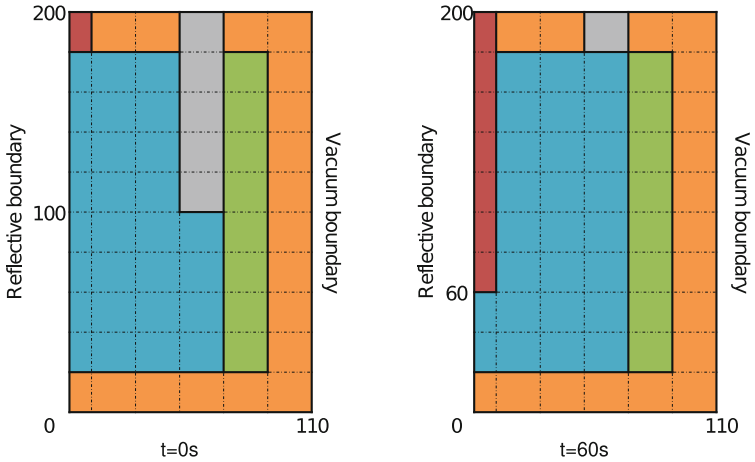


**Fig. 9.** Axial layout of the LMW problem

### 3.3 NEACRP Benchmark Problem

The NEACRP rod ejection benchmark includes two types of reactors, i. e. pressurized water reactor and boiling water reactor. It is mainly used for the verification of the neutronics-thermal hydraulics coupling codes of the light water reactor core [11]. The PWR benchmark refers to the geometric size and operating state of a typical PWR. The core consists of 157 assemblies, each measuring 21.606 cm in width. The fuel assemblies are made up of assemblies with various numbers of absorber rods and fuels with various levels of enrichment. Reflectors are set on the periphery region of the core. In the axial direction, the height of the active core is 367.3 cm. The control rod

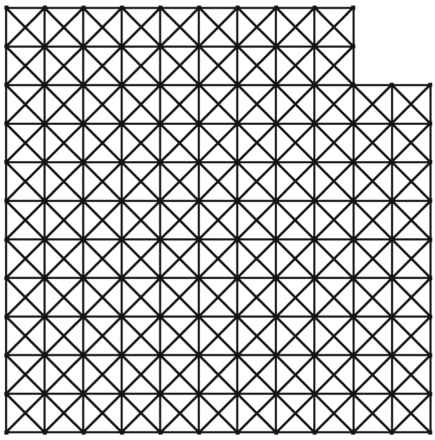

**Fig. 10.** Mesh of LMW benchmark in CENTUM

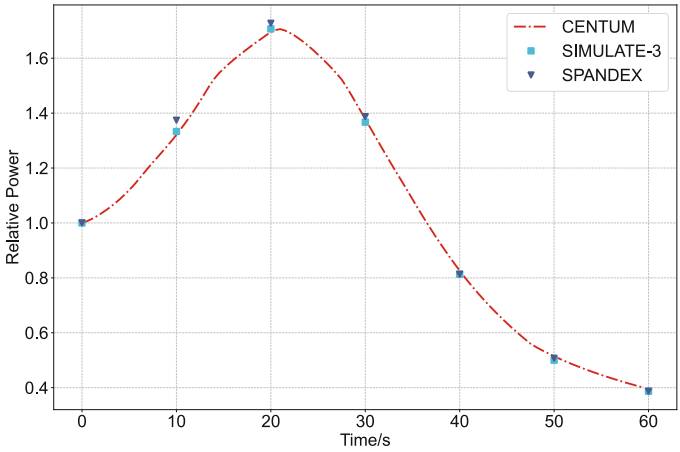


**Fig. 11.** LMW transient results

has a length of 363.195 cm, the height of the bottom of the absorbent rod when fully inserted is 37.7 cm, and the height when fully ejected is 401.183 cm. The cross section at a numerical node with control rod is determined by adding the cross section $\Delta\Sigma_{CR}$ contributed from the control rod to the cross sextion without control rod [11]:

$$\Sigma_{withCR} = \Sigma_{withoutCR} + p\Delta\Sigma_{CR} \tag{3.1}$$

where $p$ is the relative insertion in the node, i.e. $0 \leqq p \leqq 1$.

The problem contains a total of 6 operating conditions. For simplicity, we select problem A2 as an example to demonstrate the accuracy of CENTUM. Case A2 represents the HFP (hot full power, 2775 MW) condition of the reactor, and the control rods in the center position (blue area in the Fig. 13) are ejected. In case A2, the central control rod eject to the top from a height of 196.12 cm from 0 ms to 100 ms.

There are 18 layers in the axial direction, with heights of 30 cm 7.7 cm, 11 cm, 15 cm, 30 cm * 10, 12.8 cm * 2, and 8 cm, which are the same as PARCS [12] used for reference. As shown in Fig. 12, Centum is divided into a total of 790 triangular meshes in the radial direction, while PARCS is divided into 205 squares of 10.803 cm * 10.803 cm. In CENTUM's Thermal-Hydraulics Model, a fuel assembly is equivalented as a channel, Axial meshing consistent with neutronics module. The entire transient process lasts for 5 s. CENTUM sets the time-step sizes to 5 ms at 0 s–1 s and 20 ms at 1 s–5 s.

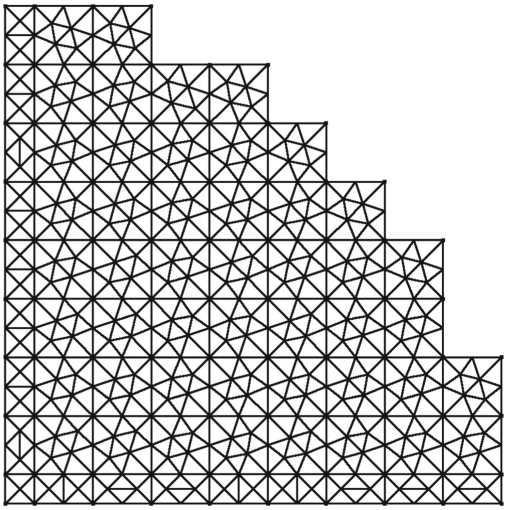

**Fig. 12.** Mesh of NEACRP benchmark in CENTUM

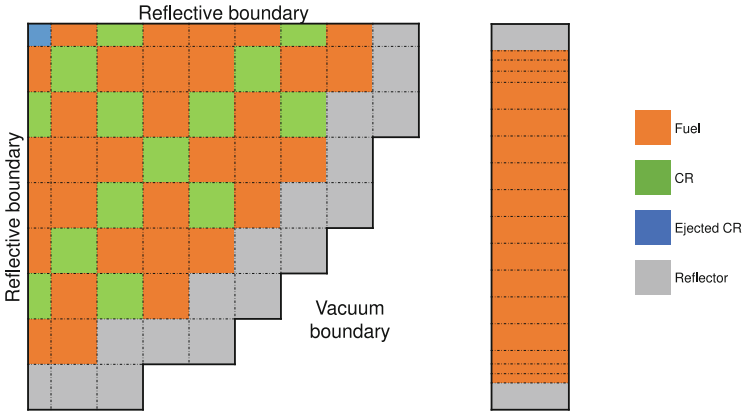


**Fig. 13.** The layout of case A2

For the steady-state coupling results, the critical boron concentration deviation of the two codes is 0.35 ppm, and the fuel average Doppler temperature deviation is 2.16 °C. Both of these are aggregate parameters of the core, so they match up well. The maximum fuel temperature difference is 30 °C. By comparing the axial power distribution in Fig. 14, it can be found that the maximum axial power of CENTUM is 0.63% higher. Figure 14 also shows the deviation of the radial power distribution, which is higher for the CENTUM outer assemblies compared to PARCS. The difference in power distribution is the most important reason for the difference in maximum fuel temperature. The transport method can better handle the various anisotropies of the angles, plus CENTUM uses a vacuum boundary condition, while PARCS uses a zero-flux boundary condition, all of which can lead to differences in the power distribution.

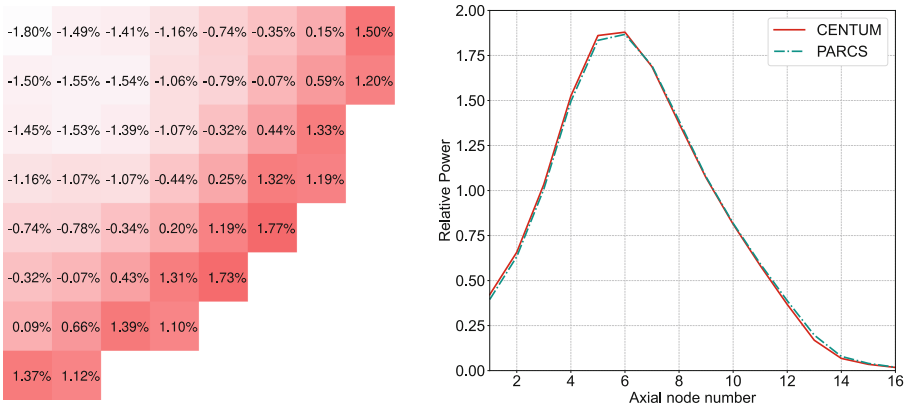


**Fig. 14.** Comparison of radial and axial power distribution between CENTUM and PARCS at steady-state

As can be seen in Fig. 15, the results of CENTUM are in good agreement with the PARCS reference solutions, with the maximum relative power deviation being 0.055%. Because CENTUM adopts the OSSI method, each neutronics calculation uses the thermal-hydraulic calculation results of the previous time step. This results in a delayed feedback to the neutronics calculation, which can also be observed in Fig. 15. The temperature rise curve of the coolant outlet is slightly deviated, which is mainly caused by the slightly different description of the coolant channel between the two codes (Table 3).

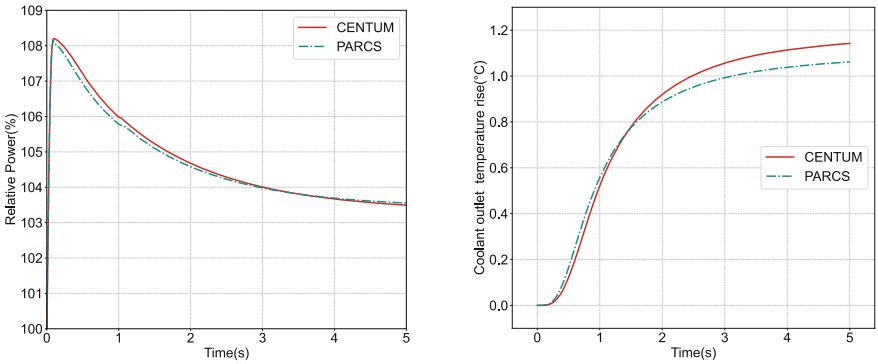


**Fig. 15.** Transient calculation results of CENTUM for A2

**Table 3.** Comparison between CENTUM and references results for case A2

| Parameter | Critical boron concentration (ppm) | Fuel maximum power (at 0 s, °C) | Average Doppler Fuel Temperature (at 0 s, °C) | Time of power peak (s) | Power peak (%) | Final coolant outlet temperature (at 5 s, °C) |
|---|---|---|---|---|---|---|
| PARCS | 1158.86 | 1672 | 546.61 | 0.09 | 108.14 | 325.03 |
| CENTUM | 1159.21 | 1702 | 548.77 | 0.1 | 108.20 | 325.80 |
| Err | 0.35 | 30 | 2.16 | 0.01 | 0.060 | 0.77 |

## 4 Conclusions

In this study, the CENTUM code is developed to analyses steady-state and transient neutronics problems using a 3D triangular-z nodal transport solver with the SCM. Meanwhile, the N-TH coupling calculation can be carried out using the multi-channel model. For neutron dynamics calculations, CENTUM agrees well with the references in the TWIGL and LMW benchmarks. The maximum errors with the TWIGL A1, A2 reference solution are −1.27% and −0.45%, respectively, when using a 20 ms time-step sizes. The maximum error with the LMW reference solution is 3.84%, and the time-step sizes set is 0.5 s. The results show that SCM can maintain good accuracy in longer time-step sizes, which can effectively reduce computing resources.

A preliminary comparison with PARCS shows that CENTUM can accurately simulate the core N-Th coupling process. It should be noted that all test cases are based on Cartesian geometry assemblies which cannot reflect the complex geometrical design of research reactors. We will preserve the verifications and applications of CENTUM on research reactors as an important research direction in the future work.

**Acknowledgements.** This research is supported by National Key R&D Program of China under grant number 2020YFB1901900, and National Natural Science Foundation of China (NSFC) [12175138].

## References


1. Zimin, V.G., Ninokata, H.: Nodal neutron Kinetics model based on nonlinear iteration procedure for LWR analysis. Ann. Nucl. Energy **25**(8), 507–528 (1998)
2. Lu, D., Guo, C., Sui, D.: A three-dimensional nodal neutron kinetics code with a higher-accuracy algorithm for reactor core in hexagonal-z geometry. Ann. Nucl. Energy **101**, 250–261 (2017)
3. Chao, Y.-A., Attard, A.: A resolution of the stiffness problem of reactor kinetics. Nucl. Sci. Eng. **90**(1), 40–46 (1985)
4. Toth, A., et al.: Analysis of Anderson acceleration on a simplified neutronics/thermal hydraulics system. Oak Ridge National Lab.(ORNL), Oak Ridge, TN (United States). Consortium for Advanced Simulation of LWRs (CASL) (2015)
5. Zhang, T., et al.: A 3D transport-based core analysis code for research reactors with unstructured geometry. Nuclear Eng. Des. **265**, 599–610 (2013)
6. Xiao, W., et al.: Application of stiffness confinement method within variational nodal method for solving time-dependent neutron transport equation. Comput. Phys. Commun., 108450 (2022)
7. Křepel, J., et al.: DYN3D-MSR spatial dynamics code for molten salt reactors. Ann. Nuclear Energy **34**(6), 449–462 (2007)
8. Ghiaasiaan, S.M., et al.: Heat conduction in nuclear fuel rods. Nucl. Eng. Des. **85**(1), 89–96 (1985)
9. Goluoglu, S.: A deterministic method for transient, three-dimensional neutron transport. The University of Tennessee (1997)
10. Ban, Y., Endo, T., Yamamoto, A.: A unified approach for numerical calculation of space-dependent kinetic equation. J. Nucl. Sci. Technol. **49**(5), 496–515 (2012)
11. Finnemann, H., et al.: Results of LWR core transient benchmarks. No. NEA-NSC-DOC-93-25. Nuclear Energy Agency (1993)
12. Joo, H.G., et al.: PARCS: a multi-dimensional two-group reactor kinetics code based on the nonlinear analytic nodal method. PARCS Manual Version **2** (1998)


**Open Access** This chapter is licensed under the terms of the Creative Commons Attribution 4.0 International License (http://creativecommons.org/licenses/by/4.0/), which permits use, sharing, adaptation, distribution and reproduction in any medium or format, as long as you give appropriate credit to the original author(s) and the source, provide a link to the Creative Commons license and indicate if changes were made.

The images or other third party material in this chapter are included in the chapter's Creative Commons license, unless indicated otherwise in a credit line to the material. If material is not included in the chapter's Creative Commons license and your intended use is not permitted by statutory regulation or exceeds the permitted use, you will need to obtain permission directly from the copyright holder.